Pergamon

Geochimica et Cosmochimica Acta, Vol. 68, No. 4, pp. 805–817, 2004

0016-7037/04 $30.00 + .00

doi:10.1016/j.gca.2003.06.002

Experimental investigation of the effect of dissolution on sandstone permeability, porosity, and reactive surface area

CARLOS F. JOVÉ COLÓN,* ERIC H. OELKERS, and JACQUES SCHOTT
Laboratoire de Géochimie, CNRS-OMP-Université Paul Sabatier, 38 Rue des Trente-Six Ponts, 31400 Toulouse, France

(*Received July* 23, 2002; *accepted in revised form June* 17, 2003)

Abstract—The temporal permeability, porosity, and reactive surface area evolution during dissolution of nonfractured/clay-free Fontainebleau sandstone cores was measured using a flow through percolation reactor. Four core dissolution experiments, each of ~1000 h duration, were performed on sandstone cores having initial porosities ranging from 5.1 to 16.6%. All experiments were performed at 80°C and at far from equilibrium conditions using a 0.1 M NaOH input solution with a calculated in situ pH of 11.4. Permeability evolution was determined using Darcy's law together with in situ measured differential pressures. Reactive surface area and porosity evolution were quantified from the mass of Si leaving the core during the experiments. The 5.1 and 8.9% initial porosity sandstone cores experienced porosity increases of 1.2 and 1.4 percent, respectively, during the experiments. These cores experienced a corresponding permeability increase from 0.27 to 0.74 mD and 0.57 to 0.87 mD, respectively. In contrast, the 10.6 and 16.6% initial porosity sandstone cores had permeabilities that were essentially constant during the dissolution experiments despite porosity increases of 6.3 and 2.5%, respectively. Only the 5.1% initial porosity core experienced a permeability evolution roughly consistent with a cubic law dependence on porosity. Reactive surface areas increased during the experiments for all cores; those for the 5.1, 10.6, and 16.6% initial porosity cores increased by $21 \pm 6\%$ for each percent porosity increase. The reactive surface area of the 8.9% initial porosity core, however, increased by 148% for each percent porosity increase. These results suggest that dissolution of the 8.9% initial porosity core opened a substantial number of isolated pores, exposing new quartz grain surfaces to dissolution. *Copyright © 2004 Elsevier Ltd*

1. INTRODUCTION

The accurate understanding of porosity, permeability, and reactive surface area is essential for quantifying chemical mass transport in natural systems. The importance of these physical rock properties to chemical mass transport have been summarized by Bredehoeft and Norton (1990), Oelkers (1996), and Jamtveit and Yardley (1997). To address this need, micron scale characterization, using techniques such as Laser Scanning Confocal Microscopy and X-ray tomography, has been applied to the three dimensional mapping of pore morphologies in the laboratory (cf. Fredrich et al., 1993, 1995; Lindquist et al., 1996; Fredrich, 1999; Mok et al., 2002). Such mapping allows direct estimation of permeability and fluid-mineral surface area. Nevertheless, because rock permeability and surface areas are properties that cannot, in most cases, be readily measured in natural systems, they are commonly approximated through phenomenological and/or empirical relations (see Lasaga, 1984; Ortoleva et al., 1987; Lichtner, 1988, 1996; Sevougian et al., 1992; Bryant et al., 1993a; Steefel and Lasaga, 1994; Oelkers et al., 1996; Steefel and MacQuarrie, 1996). For this reason, many studies have been aimed at developing algorithms, based on idealized geometries, to predict permeability and surface areas of natural porous materials (see for example Kozeny, 1927; Carman, 1937; Berryman and Blair, 1986; Doyen, 1988; Bryant and Blunt, 1992; Bryant et al., 1993a,b; Schwartz et al., 1993; Hürlimann et al., 1994; Panda and Lake, 1994; Canals and Meunier, 1995; Auzerais et al., 1996).

Towards the improved understanding of permeability and fluid mineral surface area of natural porous rocks, the first paper in this series (Kieffer at al., 1999) performed short-term dissolution experiments on Fontainebleau sandstone cores. These experiments yielded the permeability and fluid-mineral surface area as a function of core porosity and fluid flow velocity. When natural porous materials, however, are subject to dissolution and precipitation during geochemical processes, their physical properties may be heterogeneously altered. To assess the effects of dissolution on permeability and fluid-mineral surface area, long-term Fontainebleau sandstone core dissolution experiments have been performed in the present study. The purpose of this manuscript is to present the results of this study and to use them to assess the applicability of available predictive models to describe the permeability and surface areas of natural porous materials in response to dissolution reactions.

2. THEORETICAL BACKGROUND

2.1. Reactive Surface Area

Within the framework of Transition State Theory (TST), the forward or far-from-equilibrium dissolution rate (r_+) of a mineral is assumed proportional to the *reactive* or effective surface area of the mineral in contact with the aqueous solution. Such rates can be expressed as (Aagaard and Helgeson, 1977, 1982; Lasaga, 1981; Oelkers, 2001)

* Author to whom correspondence should be addressed (cfjovec@sandia.gov).

Present address: Sandia National Laboratories, Total System Performance Assessment Dept., P.O. Box 5800 MS0778, Albuquerque, NM 87185-0778, USA.

$$r_+ = \mathrm{k}_+ \mathrm{s} \prod_{\mathrm{i}=1}^{\hat{\mathrm{i}}} \frac{K_i \left(\frac{a_{\mathrm{H}^+}^{z_i}}{a_{\mathrm{M}_\mathrm{i}^{z_i+}}} \right)^{\mathrm{n_i}}}{1 + K_\mathrm{i} \left(\frac{a_{\mathrm{H}^+}^{z_i}}{a_{\mathrm{M}_\mathrm{i}^{z_i+}}} \right)^{\mathrm{n_i}}}, \quad (1)$$

where k_+ designates a reactive surface area normalized dissolution rate constant, s stands for the *reactive* surface area exposed to the aqueous solution, K_i refer to equilibrium constants for metal-proton exchange reactions, and a_i, z_i, and n_i represent the activity, charge, and the stoichiometric reaction coefficient of the *i*th aqueous species, respectively. The symbol $\mathrm{M_i}$ in Eqn. 1 corresponds to the *i*th aqueous species present in solution. When a_i for all aqueous species having nonzero n_i are constant, Eqn. 1 can be simplified to

$$\mathrm{s} = \frac{\mathrm{r}_+}{\mathrm{k'}_+}, \quad (2)$$

where $\mathrm{k'}_+$ represents a *reactive* surface area normalized dissolution rate constant defined by

$$\mathrm{k'}_+ \equiv \mathrm{k}_+ \prod_{\mathrm{i}=1}^{\hat{\mathrm{i}}} \frac{K_i \left(\frac{a_{\mathrm{H}^+}^{z_i}}{a_{\mathrm{M}_\mathrm{i}^{z_i+}}} \right)^{\mathrm{n_i}}}{1 + K_\mathrm{i} \left(\frac{a_{\mathrm{H}^+}^{z_i}}{a_{\mathrm{M}_\mathrm{i}^{z_i+}}} \right)^{\mathrm{n_i}}}.$$

If $\mathrm{k'}_+$ is known, the reactive surface area of a mineral within a core sample can be deduced from Eqn. 2 by measuring its forward dissolution rate (r_+).

It is not generally possible to quantify *reactive* surface areas in natural geochemical systems because they cannot be directly measured. Consequently, total surface areas are often used to quantify mineral dissolution rates. Total surface areas are typically determined using B.E.T. gas adsorption techniques (Brunauer et al., 1938; see also Brantley et al., 1999; Brantley and Mellott, 2000; Oelkers, 2002). Aagaard and Helgeson (1982) and Helgeson et al. (1984) noted that as mineral dissolution commonly occurs at selected sites on the reactant mineral surface, the *reactive* surface area of a mineral may be significantly less than its total surface area. They proposed a relation between these two surface areas given by

$$\mathrm{s} = \eta \zeta \mathbf{s} \quad (3)$$

where *s* refers to the total surface area of the mineral, and η and ζ correspond to the surface density and mean cross sectional area of active sites, respectively. As η and ζ may not be constant, s/**s**, and thus dissolution rates normalized to total surface area may vary 1) among various samples of the same mineral, and 2) during the long term dissolution experiments performed on a single mineral sample (cf. Gautier et al., 2001). Moreover, it should be emphasized that relations such as Eqn. 3 are a simplification of the behavior of a true mineral, which may be comprised of a variety of different surfaces each with distinct dissolution rates (e.g., Luttge et al., 1999).

In the present study, the total quartz surface areas in contact with an aqueous solution passing through Fontainebleau sandstone cores at the onset of long term dissolution experiments are generated from comparison between their dissolution rates with those of a quartz grains taken from these cores of known total surface area. In both cases, steady-state quartz dissolution rates are determined from the chemical flux removed by the aqueous fluid flowing through a reactor as a function of time in aqueous solutions for which a_i for all aqueous species having nonzero n_i are constant. This relation is given by

$$r_+ = -\frac{\partial m_{\mathrm{quartz}}}{\partial t} = \Delta C_{\mathrm{SiO_2}} Q = \mathrm{sk'}_+ = \eta \zeta \mathbf{s} \mathrm{k'}_+ \quad (4)$$

where *t* designates time, $\Delta C_{\mathrm{SiO_2}}$ refers to the difference in $\mathrm{SiO_2(aq)}$ molal concentration between the inlet and the outlet solutions at steady-state, and *Q* corresponds to the mass flow rate of the reactive fluid. m_{quartz} designates the number of moles of quartz present during the dissolution experiment. Assuming η and ζ are identical for Fontainebleau quartz grains present in a core or separated into individual grains and a_i for all aqueous species having nonzero n_i are constant, the total quartz-water interfacial surface area of a sandstone core (s_{core}) at the onset of core dissolution experiments can be determined by equating two versions of Eqn. 4, one written for core dissolution and another written for free quartz grain dissolution according to

$$s_{\mathrm{core}} = \frac{s_{\mathrm{grains}}}{r_{+,\mathrm{grains}}} \Delta C_{\mathrm{SiO_2,\,core}} Q_{\mathrm{core}}. \quad (5)$$

where the subscript 'grains' and 'core' refer to the indicated property obtained during the dissolution of the free quartz grains and sandstone core, respectively. It is customary in reactive transport modeling to use volume normalized surface areas (see for example Bear, 1972). $\bar{s}_{\mathrm{core}}$, the volume normalized total quartz-water interfacial surface area of the core can be defined by

$$\bar{s}_{\mathrm{core}} \equiv \frac{s_{\mathrm{core}}}{V_{\mathrm{core}}}, \quad (6)$$

where V_{core} designates the core volume. Note that $\bar{s}_{\mathrm{core}}$ is commonly expressed in units of length^{-1} (see Fredrich et al., 1993; Hürlimann et al., 1994; Kieffer et al., 1999).

η and ζ have been observed to vary significantly during long term quartz dissolution experiments (Gautier et al., 2001). *Reactive* surface areas and measured quartz dissolution rates during long term core dissolution experiments can, therefore, vary due to 1) changes in total quartz-water interfacial surface area, for example by the opening of isolated pores or by grain surface roughening or 2) changes in the surface site density and mean cross sectional area of active sites. Nevertheless variations in quartz *reactive* surface area can be quantified during long term core dissolution experiments by dividing two expressions of Eqn. 2, one written for the initial dissolution of the core, and one written for the dissolution of the core at time *t* to obtain

$$\frac{\mathrm{s}_t}{\mathrm{s}_0} \equiv \frac{r_{+,t}}{r_{+,0}}. \quad (7)$$

where s_0 and s_t designate the reactive surface area at the onset of the core dissolution experiment and after an elapsed time of *t*, and $r_{+,0}$ and $r_{+,t}$ denote the corresponding quartz forward dissolution rates. The quotient s_t/s_0will be used below to quantify the relative change in *reactive* surface area during long term core dissolution experiments.

Table 1. Summary of porosities, permeabilities, and total volume normalized total mineral/water interfacial surface area of the cores prior to dissolution.

Core	Head constant permeability (mD)[a]	Initial in situ permeability (mD)[b]	Absolute porosity (%)[a]	Connected porosity (%)[a]	$\bar{s}_{core}$ (cm^{-1})[b]
1	2.7	0.27	5.1	2	70.8
2	86.3	0.57	8.9	8.2	31.5
3	159	40.8	10.6	9.8	243.9
4	1010.8	66.6	16.6	15.8	104.9

[a] At 25°C, from Keiffer et al. (1999).
[b] At 80°C, This study.

2.2. Geometric Surface Area Models

Surface areas of porous media are often approximated using simple geometrical models involving the ordered arrangement or packing of spheres (Bear, 1972; Canals and Meunier, 1995). For example, the surface area of a random arrangement of spherical pores can be approximated recalling that the volume of a sphere is proportional to its diameter cubed, and its surface area is proportional to its diameter squared. A simple geometric model for describing the volume normalized total mineral-water interfacial surface area ($\bar{s}$) of a consolidated porous rock is thus given by

$$\bar{s} = \bar{s}_0 \left(\frac{\phi}{\phi_0} \right)^{2/3} \tag{8}$$

where ϕ refers to the rock porosity, and $\bar{s}_0$ stands for the volume normalized mineral-water interfacial surface area of the rock at an initial porosity of ϕ_0. Canals and Meunier (1995) proposed a more elaborate geometric model based on the assumption that the porous media is comprised of a well-sorted close-packed array of spheres that intergrow as porosity decreases. A review of the Canals and Meunier (1995) model is provided by Kieffer et al. (1999), where a close correspondence was found between this model and experimentally measured total quartz-water interfacial surface areas of Fontainebleau sandstone cores.

2.3. Porosity Evolution

The temporal porosity change during the dissolution of a pure quartz sandstone core can be evaluated from the total SiO_2 removed by the reactive fluid in accord with

$$\phi_t = \phi_0 + \frac{V_{m,\,qtz}}{V_{\text{core}}} Q \int_{t=t_0}^{t} \Delta C_{SiO_2}\, dt \tag{9}$$

where ϕ_t denotes the total core porosity at time t, ϕ_0 stands for the initial core porosity, t_0 represents the time at the start of the experiment, $V_{m,qtz}$ refers to the molar volume of quartz, and V_{core} again designates the total core volume. Eqn. 9 can be used to determine the porosity of a dissolving core by numerically integrating this equation yielding

$$\phi_t = \phi_0 + \frac{V_{m,\,qtz}}{V_{\text{core}}} Q \sum_{i} (\Delta C_{SiO_2,\,i} \Delta t_i) \tag{10}$$

where ΔC_{SiO_2},i stands for the ith experimentally measured value of ΔC_{SiO_2} and Δt_i represents the elapsed time between the ith and the $i - 1$th outlet solution sampling.

2.4. Permeability Evolution

In situ core permeabilities are computed in the present study using a simplified version of the one-dimensional Darcy's law for horizontal flow (Darcy, 1856; Bear, 1972) given by

$$k = q\mu \left(\frac{\Delta L}{\Delta P} \right) \tag{11}$$

where k designates permeability, q denotes the specific discharge of the percolating fluid, ΔP stands to the differential fluid pressure change across the core, and ΔL refers to the core length. Dynamic viscosities (μ) of the 80°C reactive aqueous electrolyte solution are calculated using the equations given by Zaytsev and Aseyev (1992), and q is computed using (Bear, 1972)

$$q = \frac{Q}{s_+ \rho} \tag{12}$$

where s_+ represents the core cross-sectional area and ρ designates the fluid density, which was taken in the present study from Akerlof and Kegeles (1939).

Many equations aimed at estimating the permeability evolution of porous materials are based on permeability/porosity correlations. A simple and commonly used correlation is given by (Doyen, 1988)

$$k = k_0 \left(\frac{\phi}{\phi_0} \right)^{n} \tag{13}$$

where k_0 stands for the permeability at the onset of the experiments at an initial porosity of ϕ_0. The exponent n is a constant, which usually 2 or greater (Aharonov et al., 1998). The commonly used cubic law is consistent with n = 3 (Bear, 1972); Doyen (1988) suggested that the best fit of data is obtained using n = 3.8.

3. EXPERIMENTAL METHODOLOGY

The dissolution experiments in the present study were performed on Fontainebleau sandstone grains and cores taken from the same ~25 × 25 cm samples studied by Kieffer et al. (1999); some physical properties of these cores are presented in Table 1. The Fontainebleau sandstone has been the subject of numerous studies aimed at characterizing relations among porosity, permeability, and elastic wave velocities (Bourbie and Zinszner, 1985; Bryant and Blunt, 1992; Bryant et al., 1993a,b; Bryant and Raikes, 1995). The composition of this sandstone was evaluated by X-Ray Riffraction (XRD) and optical microscopy indicating that this rock is essentially ~100% quartz. Small

Table 2. Summary of sample porosity, permeability, relative *reactive* surface area, and flow rate of all core experiments performed in the present study.

Elapsed time (h)	ϕ (%)	k (mD)	C_{SiO_2} ($\times 10^{-3}$ mol/kg)	s_t/s_0	In situ ΔP (bar)
CORE 1: $\phi_0 = 5.1\%$; $Q = 0.1$ gm/min; $q = 143$ m/yr, $\Delta L = 4.1$ cm					
77	5.10	0.27	1.39	1	2.42
99.53	5.12	0.27	1.38	0.99	2.49
126.97	5.13	0.26	1.34	0.96	2.59
149.37	5.16	0.26	1.32	0.94	2.54
172.49	5.19	0.27	1.39	1.00	2.49
195.12	5.22	0.27	1.44	1.04	2.44
218.99	5.25	0.29	1.50	1.08	2.33
244.59	5.29	0.30	1.61	1.16	2.22
267.85	5.32	0.30	1.68	1.21	2.19
293.99	5.36	0.32	1.81	1.30	2.06
313.32	5.39	0.33	1.72	1.23	2.04
338.13	5.43	0.34	1.84	1.32	1.95
362.32	5.47	0.35	1.83	1.32	1.88
386.08	5.51	0.36	1.74	1.25	1.87
409.58	5.55	0.37	1.76	1.26	1.78
433.98	5.59	0.38	1.84	1.32	1.74
480.86	5.67	0.40	1.86	1.34	1.64
507.16	5.71	0.41	1.81	1.30	1.63
529.5	5.74	0.40	1.78	1.28	1.66
556.58	5.79	0.40	1.72	1.24	1.65
579.16	5.82	0.48	1.67	1.20	1.37
604.03	5.86	0.47	1.77	1.27	1.41
629.11	5.90	0.51	1.66	1.19	1.30
649.99	5.93	0.45	1.74	1.25	1.47
675.99	5.97	0.46	1.69	1.21	1.43
699.99	6.00	0.53	1.74	1.25	1.26
723.35	6.04	0.56	1.74	1.23	1.18
745.83	6.07	0.58	1.71	1.23	1.14
766.28	6.11	0.60	1.64	1.18	1.11
789.61	6.14	0.60	1.67	1.20	1.11
812.08	6.18	0.74	1.77	1.27	0.90
843.96	6.23	0.56	1.78	1.28	1.18
869.63	6.27	0.71	1.87	1.35	0.94
892.59	6.31	0.74	1.84	1.32	0.90
CORE 2: $\phi_0 = 8.9$ %; $Q = 0.1$ gm/min; $q = 143$ m/yr, $\Delta L = 4.5$ cm					
0	8.90	0.57	0.68	1.00	1.29
25.23	8.91	—	0.63	0.93	—
49.72	8.92	0.60	0.69	1.01	1.21
72.27	8.94	0.60	0.76	1.12	1.21
95.25	8.95	0.58	0.76	1.12	1.26
122.9	8.96	0.62	0.75	1.10	1.17
146.93	8.98	0.60	0.75	1.10	1.22
171.92	8.99	0.57	0.78	1.15	1.29
195.47	9.01	0.54	0.82	1.21	1.35
216.83	9.02	0.57	0.88	1.29	1.29
234.67	9.03	0.52	0.83	1.22	1.40
261.67	9.05	0.52	0.85	1.25	1.40
280.17	9.06	0.54	0.91	1.34	1.36
308.67	9.08	0.54	0.99	1.46	1.36
327.67	9.10	0.55	0.90	1.32	1.33
355.17	9.12	0.55	0.89	1.31	1.34
361.62	9.12	0.55	0.97	1.43	1.34
383.75	9.14	0.54	1.09	1.60	1.35
410.87	9.16	0.56	1.05	1.54	1.31
428.59	9.18	0.58	0.98	1.44	1.25
459.37	9.20	0.58	1.00	1.47	1.27
484.15	9.22	0.56	1.05	1.54	1.30
510.67	9.25	0.52	1.06	1.56	1.40
533.29	9.27	0.58	1.10	1.61	1.31
557.13	9.29	0.53	1.24	1.82	1.38
569.52	9.30	0.54	1.17	1.72	1.35
602.02	9.33	0.55	1.07	1.57	1.33

(Continued)

Table 2. Continued

Elapsed time (h)	ϕ (%)	k (mD)	C_{SiO_2} ($\times 10^{-3}$ mol/kg)	s_t/s_0	In situ ΔP (bar)
627.42	9.35	0.59	1.08	1.59	1.24
652.07	9.38	0.61	1.10	1.62	1.19
677.87	9.40	0.59	1.08	1.59	1.23
699.89	9.43	0.57	1.30	1.91	1.29
724.33	9.45	0.55	1.37	2.01	1.32
748.07	9.48	0.56	1.40	2.06	1.30
769.02	9.50	0.62	1.39	2.04	1.19
794.57	9.53	0.58	1.34	1.97	1.25
820.8	9.56	0.57	1.32	1.94	1.29
842.27	9.58	0.59	1.31	1.93	1.25
867.52	9.61	0.62	1.42	2.09	1.18
892.44	9.64	0.59	1.38	2.03	1.22
939.89	9.70	0.64	1.36	2.00	1.15
963.29	9.73	0.63	1.57	2.31	1.16
1010.5	9.79	0.67	1.57	2.56	1.09
1032.21	9.81	0.70	1.72	2.51	1.05
1055.32	9.84	0.72	1.74	2.56	1.01
1080.67	9.88	0.76	1.71	2.51	0.96
1106.15	9.91	0.81	1.62	2.38	0.90
1126.87	9.94	0.76	1.84	2.71	0.96
1148.22	9.97	0.81	1.75	2.57	0.90
1177.57	10.01	0.78	1.80	2.65	0.94
1200.3	10.04	0.85	1.87	2.75	0.86
1292.21	10.18	0.87	1.98	2.91	0.84
CORE 3 $\phi_0 = 10.6$ %; $Q = 0.5$ gm/min; $q = 715$ m/yr, $\Delta L = 3.98$ cm					
0	10.60	40.8	0.93	1.00	0.075
22.56	10.68	40.8	0.82	0.87	0.075
49.67	10.79	40.8	0.95	1.01	0.075
70.48	10.88	40.8	0.96	1.03	0.075
94.97	10.99	40.8	1.00	1.07	0.075
96.25	11.00	40.8	1.03	1.11	0.075
144.6	11.24	40.8	1.15	1.23	0.075
169.38	11.37	40.8	1.15	1.23	0.075
189.42	11.47	40.8	1.11	1.19	0.075
217.57	11.62	40.8	1.20	1.28	0.075
241.45	11.75	40.8	1.22	1.31	0.075
266.5	11.88	40.8	1.26	1.35	0.075
288.23	12.00	43.7	1.24	1.33	0.07
316.63	12.17	43.7	1.31	1.40	0.07
339.72	12.31	43.7	1.37	1.47	0.07
359.77	12.43	43.7	1.41	1.51	0.07
381.22	12.56	43.7	1.38	1.47	0.07
406.42	12.72	43.7	1.39	1.49	0.07
428.5	12.86	43.7	1.39	1.49	0.07
502.62	13.35	43.7	1.52	1.62	0.07
521.92	13.48	43.7	1.45	1.55	0.07
618.1	14.13	43.7	1.54	1.65	0.07
640.22	14.29	47.1	1.62	1.73	0.065
660.37	14.43	47.1	1.65	1.77	0.065
690.55	14.67	47.1	1.76	1.89	0.065
711.9	14.82	47.1	1.64	1.76	0.065
738.19	15.02	47.1	1.68	1.80	0.065
758.92	15.17	47.1	1.61	1.72	0.065
784.97	15.33	47.1	1.39	1.48	0.065
810.15	15.50	47.1	1.60	1.71	0.065
835.32	15.68	47.1	1.62	1.72	0.065
880.25	15.99	47.1	1.55	1.66	0.065
905.92	16.18	47.1	1.63	1.75	0.065
926.87	16.32	47.1	1.60	1.72	0.065
953.5	16.56	47.1	2.01	2.15	0.065
976.24	16.74	47.1	1.83	1.96	0.065
999.26	16.93	47.1	1.81	1.94	0.065
1024.33	17.13	47.1	1.80	1.93	0.065
1047.54	17.32	47.1	1.90	2.04	0.065
1096.38	17.73	51.0	1.91	2.05	0.060
1119.61	17.92	51.0	1.76	1.88	0.060
1144.88	18.13	51.0	1.97	2.10	0.060
1168.94	18.35	51.0	2.05	2.19	0.060

(Continued)

Table 2. Continued

Elapsed time (h)	ϕ (%)	k (mD)	C_{SiO_2} ($\times 10^{-3}$ mol/kg)	s_t/s_0	In situ ΔP (bar)
CORE 4: ϕ_0 = 16.64 %; Q = 1.0 gm/min; q = 1430 m/yr, ΔL = 3.90 cm					
49.89	16.64	66.6	1.96	1.00	0.095
72.10	16.68	70.3	1.99	1.01	0.09
98.31	16.73	70.3	2.15	1.09	0.09
120.91	16.78	70.3	2.32	1.18	0.09
144.49	16.85	70.3	3.14	1.60	0.09
169.09	16.89	70.3	2.10	1.07	0.09
194.97	16.94	66.6	1.96	1.00	0.095
216.06	17.00	66.6	3.07	1.57	0.095
243.96	17.06	70.3	2.59	1.32	0.09
262.82	17.10	70.3	2.38	1.21	0.09
313.14	17.21	70.3	2.49	1.26	0.09
337.66	17.27	70.3	2.40	1.22	0.09
386.14	17.37	66.6	2.49	1.27	0.095
432.39	17.48	70.3	2.56	1.30	0.09
483.16	17.58	66.6	2.28	1.16	0.095
532.07	17.68	66.6	2.19	1.11	0.095
579.49	17.79	66.6	2.52	1.28	0.095
603.19	17.84	63.2	2.34	1.19	0.1
626.59	17.89	60.2	2.56	1.30	0.105
651.31	17.94	60.2	2.51	1.28	0.105
669.67	17.98	60.2	2.31	1.18	0.11
745.47	18.19	60.2	3.00	1.53	0.105
772.31	18.25	60.2	2.65	1.35	0.11
818.04	18.37	60.2	3.01	1.54	0.11
865.97	18.49	60.2	2.74	1.40	0.11
913.47	18.62	60.2	3.05	1.55	0.11
937.34	18.68	60.2	3.04	1.55	0.11
962.27	18.75	60.2	3.09	1.57	0.11
984.62	18.81	—	3.03	1.55	—
1010.24	18.88	60.2	2.97	1.51	0.115
1034.47	18.95	59.4	3.00	1.53	0.105
1057.57	19.01	57.4	2.78	1.42	0.11
1082.87	19.07	54.9	2.87	1.47	0.115
1106.79	19.13	57.4	2.82	1.44	0.11

amounts ($\ll$1%) of muscovite and an unidentified clay material were observed in samples with porosities $\geq$10%.

The two reactor systems used in the present study are identical to those used by Kieffer et al. (1999). Quartz dissolution rates of Fontainebleau sandstone grains were measured using a mixed-flow reactor. The use and application of this type of reactor to dissolution experiments have already been described in detail by Berger et al. (1994), Gautier et al. (1994), and Kieffer et al. (1999). The input solution for this experiment was injected into the mixed flow reactor at a flow rate of 0.1 g/min using a single-piston Gilson pump. The quartz grains used in this experiment were obtained from the same sandstone samples as the cores used during the dissolution experiments described below. These grains were removed by hand from the sandstone. Uncrushed grains were sieved to a mesh size of 125 to 250 μm and cleaned ultrasonically with methanol. The BET surface area of the resulting powder, as measured using Kr as the adsorbing gas, was 0.0634 $\pm$ 0.0013 m^2/g. Six grams of this powder were used in this quartz grain dissolution experiment.

Long term dissolution of four Fontainebleau sandstone cores, each 2.2 cm in diameter and from 3.9 to 4.5 cm in length, was conducted in the externally-heated single-pass percolation cell; a schematic illustration and a detailed description of this reactor, and the experimental techniques used in this study are provided by Kieffer et al. (1999). The input solution was injected into this reactor at flow rates of 0.1, 0.5, and 1 g/min with a single piston Gilson pump (Table 2). Percolation experiments were initiated at 25°C. Air bubbles, which could potentially block pore throats, were removed using a CO_2 flooding technique. The core was first flooded with CO_2. This gas was subsequently removed using a vacuum pump and the input solution was pumped into the percolation cell at a constant fluid flow rate until a stable differential pore pressure was achieved. This CO_2 flooding cycle was repeated 4–5 times. As CO_2 is highly soluble, this flooding process assures that none of the pore spaces or throats will be occupied by gas bubbles. The reactor was subsequently heated to 80°C and fluid flow continued until the differential pressure attained a constant value. Outlet solution samples were taken regularly and fluid flow rates were held constant throughout each experiment.

Input solutions for both the grain and core dissolution experiments were prepared from either concentrated reagent-grade Merck Titrisol NaOH solution or reagent grade Prolabo Normapur NaOH pellets diluted in double-distilled (MilliQ) water to produce a 0.1 m NaOH solution with pH=13 at 25°C. Outlet solutions were analyzed for total Si and pH. Si concentrations in the outlet solutions were measured using the blue Molybdate method (Koroleff, 1976). pH of inlet and outlet solutions at 25°C was measured using a Schott combination electrode. The quench pH of all inlet and outlet solutions was 13$\pm$0.02 pH. To verify the Al content in the outlet solutions, some fluid samples were analyzed by graphite furnace atomic absorption spectroscopy using a Perkin-Elmer 5100 PC atomic absorption spectrophotometer. The concentration of dissolved Al in these solutions never exceeded the detection limit of 1×10^{-3} ppm. This observation indicates that the addition of Si due to aluminosilicate dissolution was insignificant. The recalculated in situ pH of 11.4 at 80°C was obtained using the computer code package EQ3NR (Wolery, 1983; Wolery, 1992; Wolery and Daveler, 1992). This use of an alkaline solution was adopted for two reasons: 1) quartz dissolution rates are higher in alkaline pH solutions,

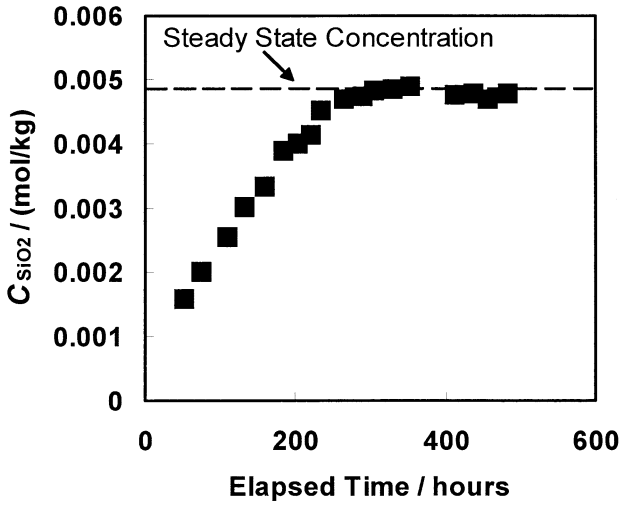

Fig. 1. Temporal evolution of outlet fluid SiO_2 concentration during Fontainebleau sandstone grain dissolution experiments. This grain dissolution experiment was performed in a mixed flow reactor at 80°C in a 0.1 mol/kg NaOH aqueous solution. The symbols correspond to measured solution concentrations and the dashed line to the steady-state limit. Results of this experiment are used to determine the BET normalized dissolution rate of the Fontainebleau sandstone used in the present study (see text).

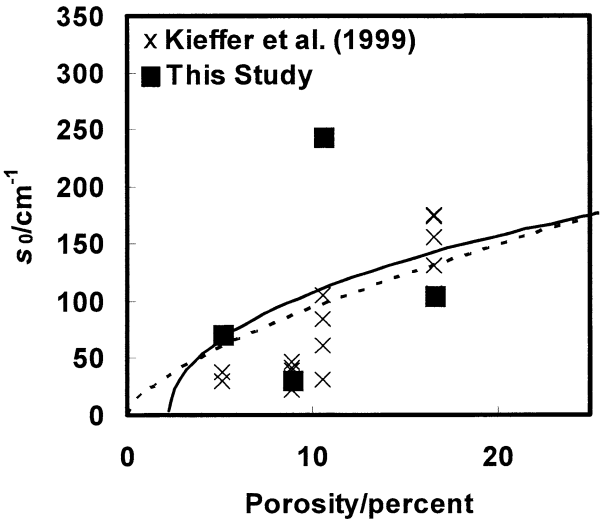

Fig. 2. Variation of volume normalized total quartz interfacial surface area of Fontainebleau sandstone cores. The filled squares correspond to surface areas of the cores at the onset of the dissolution experiments performed in the present study, whereas the symbols x designate values reported by Kieffer et al. (1999). The solid and dashed curves correspond to predictions made using geometric models provided by Canals and Meunier (1995) and using Eqn. 8, respectively, assuming a 250 quartz grain diameter and closest sphere packing leading to = 177.7 cm^{-1} at =25.95%.

which results in measurable quantities of aqueous Si in the outlet solutions and 2) to prevent the presence of a positive surface charge on potential colloidal or fine particles that could stick electrostatically to negatively charged quartz surfaces. Such an effect could impede fluid flow through small pore channels.

4. RESULTS AND DISCUSSION

The temporal evolution of measured outlet solution SiO_2 concentrations during the quartz grain dissolution experiments performed in a mixed flow reactor is illustrated in Figure 1. It can be seen in this figure that a steady-state outlet SiO_2 concentration is achieved after ~400 h. The quartz dissolution rate obtained in this experiment was 8×10^{-9} mol/s, which corresponds to a BET surface area normalized quartz rate of 2.10×10^{-12} mol/(cm^2 s). This value is ~4 times higher than that calculated for this temperature, pH, and Na concentration using the equations of Dove (1994). The difference between rates obtained in the present study and those of Dove (1994) may stem from the identity of the quartz grains studied. The grains dissolved in the present study are covered with quartz cement precipitated in a sedimentary basin. In contrast, Dove (1994) studied crushed cleaned quartz of hydrothermal origin.

Quartz grain dissolution rates obtained in the present study were used together with Eqns. 5, and 6, and aqueous SiO_2 concentrations and fluid flow rates listed in Table 2 to generate the volume normalized total quartz-water interfacial surface areas of the sandstone cores ($\bar{s}_{core}$) at the onset of the experiments listed in Table 1. Note the quartz dissolution rates used for this calculation were normalized to B.E.T. surface areas measured before the dissolution experiment. This was done so that the computed $\bar{s}_{core}$ would correspond to that of the core before quartz dissolution. Resulting surface areas are illustrated in Figure 2, where it can be seen that they are within a factor of ~3 of those reported by Kieffer et al. (1999) and geometric model estimates. Differences between $\bar{s}_{core}$ values obtained in the present study and corresponding values of Kieffer et al. (1999) illustrate the degree of heterogeneity of this sandstone, as the corresponding cores were cut from single ~25 × 25 cm sandstone samples. $\bar{s}_{core}$ values obtained in the present study are also within a factor of ~2 of corresponding values determined from Laser Scanning Confocal Microscopy by Fredrich et al. (1993) and Mok et al. (2002) and from X-Ray tomography by Lindquist et al. (1996).

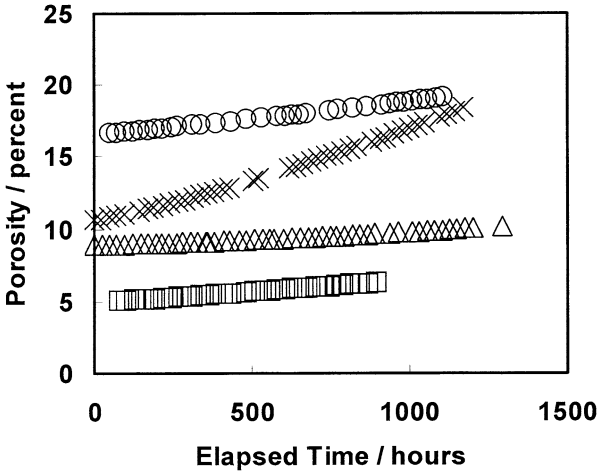

Fig. 3. Temporal porosity evolution during the Fontainebleau sandstone core dissolution experiments performed during the present study. The open squares, triangles, crosses and circles refer to results obtained for cores 1, 2, 3, and 4, respectively.

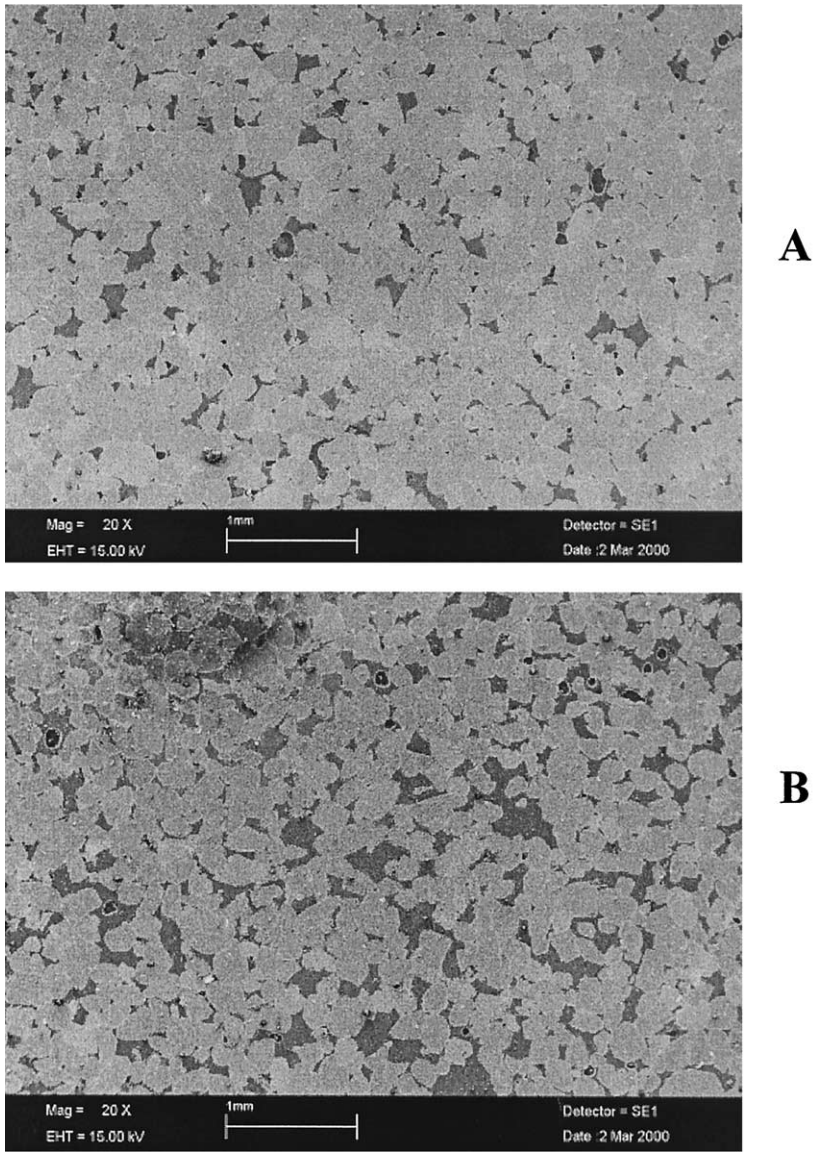

Fig. 4. Photomicrographs of core sample 3 (A) before and (B) following its dissolution in the core reactor. The scale is bar is provided in the figure.

Experimentally determined permeability, porosity, and relative reactive surface area (s_t/s_0) during the Fontainebleau sandstone dissolution as a function of elapsed time are reported in Table 2. Permeabilities were generated from measured in situ differential pressures using Eqns. 11 and 12. Porosities and s_t/s_0 values given in this table were computed from measured outlet silica concentrations using Eqn. 10 and Eqn. 7, respectively.

The temporal porosity evolutions of the four cores during the experiments are depicted in Figure 3. All cores experienced a continuous porosity increase during the experiments. The overall porosity increase during the experiments for samples 1, 2, 3, and 4, which had initial porosities of 5.1, 8.9, 10.6, and 16.6% were 1.2, 1.4, 6.3, and 2.5%, respectively. As all reactive fluids were the same temperature, pH, and Na concentration, and highly undersaturated with respect to quartz, these different porosity increase rates are attributed in the present study to the distinct surface areas of each core. For example, the 10.6% initial porosity core apparently dissolves at a faster rate then the other three cores, which is consistent with its relatively high quartz-water interfacial surface area. Although this surface area is larger than that of the other three cores considered in this study, it is only ~2.5 greater than that estimated using geometric surface area models—see Figure 2.

Photomicrographs were taken of the full cross section of core sample 3 before and following the percolation experiments. Representative examples are illustrated in Figure 4. Quartz grain size and porosity distribution appear to be homogeneous on the ~2mm scale. The porosity of this sample was measured from 10 distinct 5×5 mm areas of these photomicrographs using the VISLOG image analysis software package. The measured porosity of the 5 × 5 mm sections of the initial core ranged from 7.03 to 8.63%, whereas those of the postexperi-

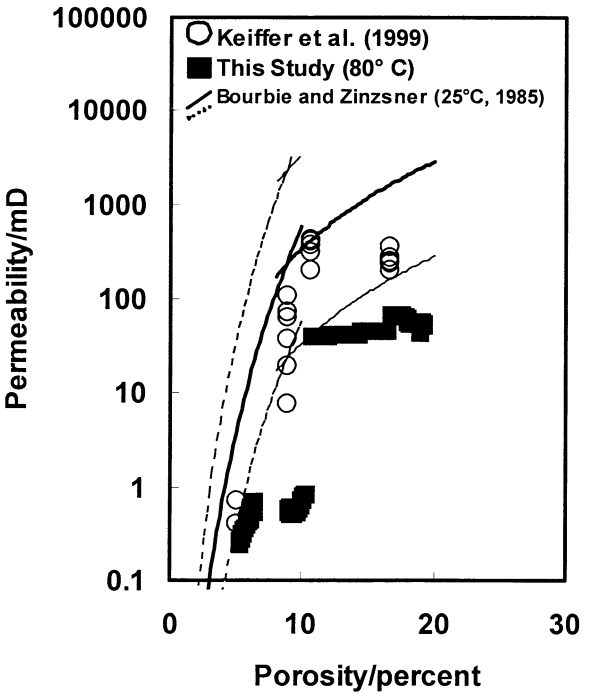

Fig. 5. In situ permeability and air permeability as a function of porosity. The solid curves represent 25°C values reported by Bourbie and Zinszner (1985). The dashed curves correspond to the reported scatter among their permeability values. Open circles are 80°C in situ permeability values reported by Kieffer et al. (1999), and solid squares delineate 80°C in situ permeabilities obtained in the present study during long term dissolution experiments.

ment core ranged from 13.2 to 15.8%. Two conclusions can be drawn from these observations. First, these observations suggest the dissolution was fairly homogeneous during the long-term experiments. Secondly, although initial core porosities measured by image analysis are 2 to 3% lower than that estimated from density differences, the porosity increase due to quartz dissolution measured by image analysis is ~6–7%. This value matches fairly closely the 7.7% increase computed from outlet aqueous SiO_2 concentration.

The variations of measured in situ permeabilities of all dissolving cores are compared with those of Bourbie and Zinszner (1985) and of Kieffer et al. (1999) in Figure 5. Permeabilities obtained in the present study are somewhat lower than those reported by Bourbie and Zinszner (1985). One reason why permeabilities measured in the present study may be on average lower is that measurements were performed in the present study at 80°C whereas those of Bourbie and Zinszner (1985) stem from 25°C measurements. Increasing temperature and associated mineral expansion leads to smaller pore throats and thus lower permeability (cf. Shmonov et al., 1995). The permeability evolution as a function of porosity during the core dissolution experiments can be assessed with the aid of Figure 6. Permeabilities of the low porosity cores (samples 1 and 2) increase with increasing porosity. Permeabilities of the high porosity cores (samples 3 and 4), however, remained essentially constant during the experiments. These permeability variations can be compared to those predicted with Eqn. 13 using n = 3 (traditional cubic law) and n = 3.8 (proposed by Doyen, 1988). Predicted permeability evolutions correspond reasonable well with their measured counterparts only for the lowest porosity core. The permeabilities of the other cores tend to be lower than that predicted using these empirical equations. This slow increase of permeability with increasing porosity suggests that the bulk of the dissolution is occurring in the pores rather than the pore channels.

The contrasting effects on permeability of dissolution within a pore versus a pore throat can be illustrated using the example shown in Figure 7. This figure shows a 0.5 mm diameter core containing a single fluid pathway comprised of a two equal length smooth circular sections, one having a 0.1 mm diameter and the other a 0.2 mm diameter. According to the Hagen-Poiseuielle law, the permeability of a core containing a single smooth circular cross sectioned pathway is given by (Bird et al., 1960)

$$k = \phi \frac{r_t^2}{8} \tag{14}$$

where r_t refers to the radius of the circular pathway. This Hagen-Poiseuille law has been used for estimating permeability of porous media within the framework of pore network models (Sisavath et al., 2001; Lock et al., 2002). The latter of these two studies generated permeabilities that were comparable to those obtained from image analysis of natural porous rocks. Eqn. 14 implies that the permeability of the part of the core having a 0.1 mm diameter is 12.7 darcys and that having a 0.2 mm diameter pathway is 202.6 darcys. Note that 1 darcy = 0.987×10^{-12} m^2. The overall permeability of the core can be computed using (Leonards, 1962)

$$k = \frac{\sum_i L_i}{\sum_i \left(\frac{L_i}{k_i}\right)} \tag{15}$$

where L_i and k_i refer to the length and permeability of the ith core segment. The core illustrated in Figure 7, therefore has an overall permeability of 24 darcys. The effect of dissolution in a pore or in pore throat can be illustrated by computing the overall permeability of this core after increasing the diameter of the 0.2 mm or 0.1 mm, respectively, section of the channelway. The results of this calculation are depicted in Figure 8. Increasing the diameter in the 0.2 mm section of channelway increases only negligibly the total core permeability; a 4% porosity increase confined to this section of channelway increases the overall permeability from 24 to 24.9 darcys. In contrast, if this dissolution was confined to the 0.1 mm channelway section, a 4% porosity increase would lead to an increase from 24 to 150 darcys. These results are compared to predictions made using Eqn. 13, where it can be seen that the pore throat dissolution leads to higher permeability increases than that estimated using these empirical models, whereas pore dissolution lead to a far slower permeability increase.

The variation of *reactive* surface area during these dissolution experiments can be evaluated using Figure 9. *Reactive* surface areas increase significantly during the experiments. Core samples 1, 3, and 4 exhibited a 21±6% surface area increase for each percent porosity increase. These values are

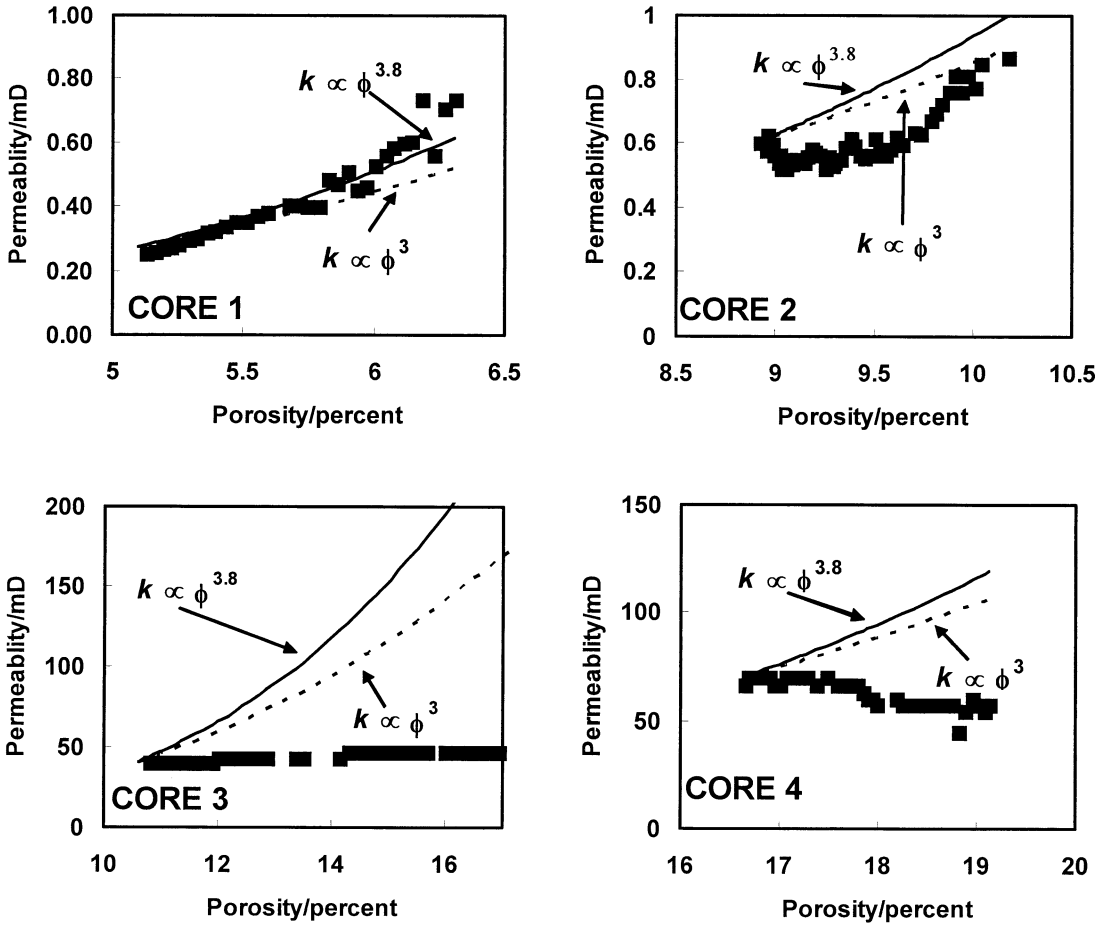

Fig. 6. In situ permeabilities (k) as a function of porosity for core samples 1 to 4 measured in the present study during long term dissolution experiments. The solid squares represent measured k values, the solid curve illustrates permeability estimates made using $k \propto \phi^{3.8}$ (after Doyen, 1988), and the dashed line corresponds to permeability estimates made assuming a cubic law dependence of permeability on porosity ($k \propto \phi^3$) (see text).

somewhat greater than those predicted with the simple geometric models described above, which range from 2.5% for core sample 4 to 15% for core sample 1. The larger measured values may stem from the fact that the dissolution may not be homogeneous and/or may tend to roughen the quartz grains that comprise the sandstone; this is in contrast with geometric models based on the assumption that all grains have smooth surfaces. Core sample 2, however, exhibited a 148% increase in *reactive* surface area for each percent porosity increase. This dramatically large effect may stem from the opening of new pore voids by quartz dissolution in this 8.9% initial porosity core. According to the cementation/compaction model of Bryant et al. (1993a), a homogeneous quartz sandstone, such as the Fontainebleau, will experience the inception of pore throat blocking at $\phi \approx 10\%$. It therefore seems likely that the slight dissolution of pore filling cement of the 8.9% initial porosity sandstone core would expose isolated pores to dissolution. Cores having higher initial porosities, such as samples 3 and 4, would have essentially all pore throats open, and thus all pores would be in contact with the reactive fluid from the beginning of dissolution. In contrast, cores with significantly lower porosity, such as sample 1 would have a large amount of cement blocking its pore throats; the dissolution of only 1–2% of the quartz from this sandstone would be insufficient to expose isolated pores to dissolution.

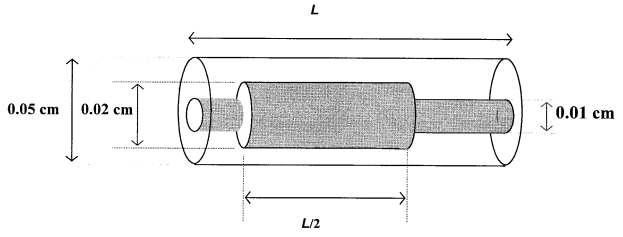

Fig. 7. Schematic illustration of a 0.5 mm diameter core containing a single channel way; see text.

Uncertainties in computed premeabilities, porosities, total quartz-water interfacial surface areas ($\bar{s}_{core}$), and relative reactive surface area (s_t/s_0) stem from uncertainties in measured

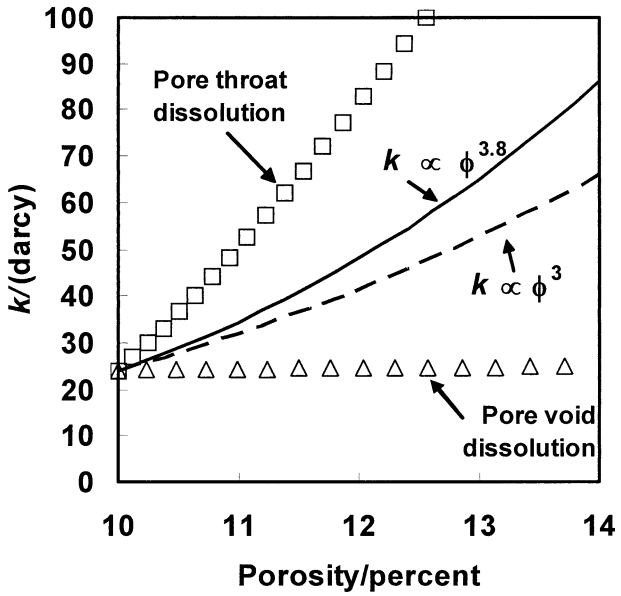

Fig. 8. Computed permeabilites of the core illustrated in Figure 7 as a function of porosity during its dissolution. The open squares and triangles correspond to results for dissolution restricted in the pore throat (0.05 mm radius channel way section) and the pore void (0.1 mm radius channel way section). The dashed and solid curves illustrate estimates made using Eqn. 13 assuming n = 3 and 3.8, respectively; see text.

outlet aqueous SiO_2 concentration, mass flow rates, differential fluid pressures, and BET surface areas. Uncertainties associated with aqueous Si concentrations obtained from colorimetry in the present study are ± 4% and those associated with determination of the mass flow rate are ±2%. Uncertainties of measured differential fluid pressures and measured BET surface areas are on the order of ±10%. It follows that the overall uncertainties associated with values of k, ϕ, $\bar{s}_{core}$, and s_t/s_0 reported in the present study are on the order of ±15%. It should be emphasized, however, that due to fine scale heterogeneities within natural sandstones, the identical experiment performed on a different core cut from the same sandstone sample may be far greater. For example, corresponding $\bar{s}_{core}$ values reported in the present study differ by those of Kieffer et al. (1999) by as much as a factor of 3. Similarly, Bourbie and Zinszner (1985) found that permeabilities of corresponding Fontainebleau sandstone cores may differ by an order of magnitude or more.

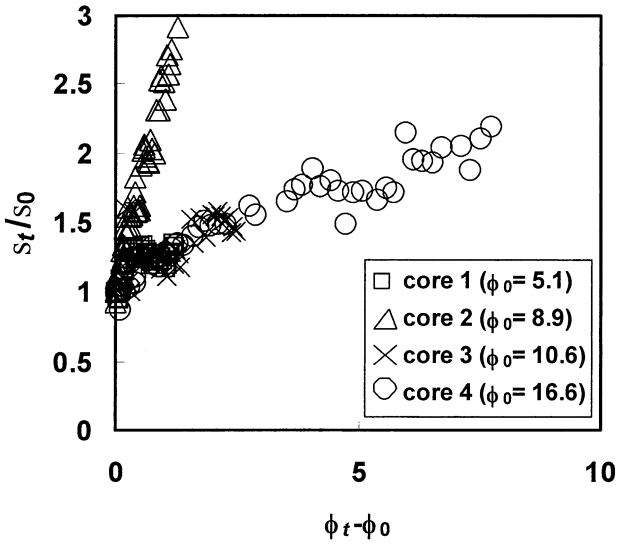

Fig. 9. Relative reactive surface area (s_t/s_0) evolution as a function of porosity increase (ϕ_t-ϕ_0) during the core dissolution experiments. The open squares, triangles, crosses, and circles refer to results obtained for cores 1, 2, 3, and 4, respectively.

5. CONCLUSIONS

The response to dissolution of the permeability and reactive surface area of Fontainebleau sandstone has been studied on four core samples with initial porosities ranging from 5 to 17%. Only the lowest porosity core exhibited permeability evolutions that are consistent within uncertainty with either the traditional cubic law of porosity ($k \propto \phi^3$) or that proposed by Doyen (1988) ($k \propto \phi^{3.8}$). Higher porosity cores had permeabilities that increase far slower than would be estimated with these simple models. The permeability of the highest porosity cores did not increase significantly during the experiments. This observation may be the result of dissolution occurring primarily in the pores rather than in pore throats. Such is likely the case for many porous rocks as the bulk of the mineral-fluid interfacial surface area is contained in the pores rather than pore throats.

Reactive surface areas of cores having initial porosities either less than 8% or more than 10% increased 21±6% for each percent porosity increase due to quartz dissolution. The core having an initial porosity of 8.9% had reactive surface areas that increased at a much greater rate with dissolution. This is interpreted to stem from the relatively little amount of cement required to be removed to expose isolated pores to the reactive fluid.

Acknowledgments—We thank Dr. Bernard Zinszner of the Institut Français du Pétrole (IFP) for generously providing the Fontainebleau sandstone samples used in this study. We are also grateful to Christophe Guy and Hélène Serra of the 'Commissariat d'Energie Atomique' (CEA) of France for generously providing the experimental apparatus and technical assistance in the course of this study. This work greatly benefited from the assistance of Bruno Kieffer who jointly collaborated with the senior author in these percolation experiments. We would also like to thank Christian Saccareau for conducting porosity and air permeability measurements on the Fontainenbleau sandstone samples. Denis Suida from the Institut Français du Pétrole (IFP) provided essential guidance concerning technical modifications for the percolation apparatus needed to conduct the in situ permeability measurements. We also thank Stephan Köhler, Stacey Callahan, Jean-Marie Gautier, Jocelyn Escalier, Jean-Claude Harrichoury, Patricia Fournier, Oleg Pokrovski, Jérôme Viers, Samuel Deberdt, Johnny Tapia, Tommaso Tosiani, and Gilles Berger for helpful discussions and encouragement during this study. The senior author gratefully acknowledges the NSF-NATO and Chateaubriand (government of France) postdoctoral fellowships for providing financial support during the course of this study at the 'Laboratoire de Géochimie' of the Université Paul Sabatier-CNRS-OMP, Toulouse, France.

Associate editor: R. A. Wogelius

REFERENCES

Aagaard P. and Helgeson H. C. (1977) Thermodynamic and kinetic constraints on the dissolution of feldspars. *Geol. Soc. Am. Abstr.* **9,** 873.

Aagaard P. and Helgeson H. C. (1982) Thermodynamic and kinetic constraints on reaction rates among minerals and aqueous solutions: I. Theoretical considerations. *Am. J. Sci.* **282,** 237–285.

Aharonov E., Tenthorey E., and Scholz C. H. (1998) Precipitation, sealing, and diagenesis 2. Theoretical analysis. *J. G. R.* **103,** 23, 969–23,981.

Akerlof G. C. and Kegeles G. (1939) The density of aqueous solutions of sodium hydroxide. *Am. Chem. Soc. J.* **61,** 1027–1032.

Auzerais F. M., Dunsmuir J., Ferréol B. B., Martys N., Olson J., Ramakrishnan T. S., Rothman D. H., and Schwartz L. M. (1996) Transport in sandstone: A study based on three dimensional microtomography. *Geophys. Res. Lett.* **23,** 705–708.

Bear J. (1972) *Dynamics of Fluids in Porous Media*. Elsevier.

Berger G., Cadoré E., Schott J., and Dove P. (1994) Dissolution rate of quartz in Pb and Na electrolyte solutions. Effect of the nature of surface complexes and reaction. *Geochim. Cosmochim. Acta* **58,** 541–551.

Berryman J. G. and Blair S. C. (1986) Use of digital image analysis to estimate fluid permeability of porous materials, I. Application of two-point correlation functions. *J. Appl. Phys.* **60,** 1930–1938.

Bird R. B., Steward W. E., and Lightfoot E. N. (1960) *Transport Phenomena*. Wiley.

Bourbie T. and Zinszner B. (1985) Hydraulic and acoustic properties as a function of porosity in Fontainebleau sandstone. *J. Geophys. Res.* **90,** 11524–11532.

Brantley S. L., White A. F., and Hodson M. E. (1999) Surface area of primary silicate minerals. In *Growth and Dissolution in Geosystems* (eds. B. Jamtveit and P. Meakin), pp. 291–326. Kluwer.

Brantley S. L. and Mellott N. (2000) Surface area and porosity of primary silicate minerals. *Am. Min.* **85,** 1767–1783.

Bredehoeft J. D. and Norton D. L. (1990) Mass and energy transport in deforming Earth's crust. In *The Role of Fluids in Crustal Processes Studies in Geophysics*, pp. 27–41. National Research Council.

Bryant S. L. and Blunt M. (1992) Prediction of relative permeability in simple porous media. *Physical Rev. A* **46,** 2004–2011.

Bryant S. L., Cade C., and Mellor D. (1993a) Permeability prediction from geologic models. *AAPG Bull.* **77,** 1338–1350.

Bryant S. L., King P. R., and Mellor D. W. (1993b) Network model evaluation of permeability and spatial correlation in a real random sphere packing. *Transport Porous Media* **11,** 53–70.

Bryant S. L. and Raikes R. (1995) Prediction of elastic-wave velocities in sandstones using structural models. *Geophysics* **60,** 437–446.

Brunauer S., Emmet P. H., and Teller E. (1938) The absorption of gases in multimolecular layers. *J. Am. Chem. Soc.* **60,** 309–319.

Canals M. and Meunier J. D. (1995) A model for porosity reduction in quartzite reservoirs by quartz cementation. *Geochim. Cosmochim. Acta* **59,** 699–709.

Carman P. C. (1937) Fluid flow through granular beds. *Trans. Inst. Chem. Eng.* **15,** 150–166.

Darcy H. (1856) *Les fontaines publique de la ville de Dijon*. Dalmont.

Dove P. M. (1994) The dissolution kinetics of quartz in sodium chloride solutions at 25° to 300°. *Am. J. Sci.* **294,** 665–712.

Doyen P. M. (1988) Permeability, conductivity, and pore geometry of sandstone. *J. Geophys. Res.* **93,** 7729–7740.

Fredrich J. T. (1999) 3D imaging of porous media using laser scanning confocal microscopy with application to microscale transport processes. *Phys. Chem. Earth* **24,** 551–561.

Fredrich J. T., Greaves K. H., and Martin J. W. (1993) Pore geometry and transport properties of Fontainebleau sandstone. *Int. J. Rock Mech. Min. Sci.* **30,** 691–697.

Fredrich J. T., Menendez B., and Wong T. F. (1995) Imaging the pore structure of geomaterials. *Science* **268,** 276–279.

Gautier J. M., Oelkers E. H., and Schott J. (1994) Experimental study of K-feldspar dissolution rates as a function of chemical affinity at 150°C and pH 9. *Geochim. Cosmochim. Acta* **58,** 4549–4560.

Gautier J. M., Oelkers E. H., and Schott J. (2001) Are quartz dissolution rates proportional to BET surface areas? *Geochim. Cosmochim. Acta* **65,** 1059–1070.

Helgeson H. C., Murphy W. M., and Aagaard P. (1984) Thermodynamic and kinetic constraints on reaction rates among minerals and aqueous solutions. II. Rate constants, effective surface area, and the hydrolysis of feldspar. *Geochim. Cosmochim. Acta.* **48,** 2405–2432.

Hürlimann M. D., Helmer K. G., Latour L. L., and Sotak C. H. (1994) Restricted diffusion in sedimentary rocks. Determination of surface-area-to-volume ratio and surface relaxivity. *J. Magnetic. Reson.* **111,** 169–178.

Jamtveit B. and Yardley W. D. (1997) Fluid flow and transport in rocks: An overview. In *Fluid Flow and Transport in Rocks—Mechanisms and Effects* (eds. B. Jamtveit and W. D. Yardley), pp. 1–14. Chapman and Hall.

Kieffer B., Jove C. F., Oelkers E. H., and Schott J. (1999) An experimental study of the reactive surface area of the Fontainebleau sandstone as a function of porosity, permeability, and fluid flow rate. *Geochim. Cosmochim. Acta* **63,** 3525–3534.

Koroleff F. (1976) Determination of silicon. In *Methods of Seawater Analysis* (ed. Grasshoff), pp. 149–158. Springer Verlag.

Kozeny J. (1927) Uber kapillare Leitung des Wassers im Boden. *Sitzungber. Oesterr. Akad. Weiss. Math. Naturwiss. Kl. Abt/2a, 1,* **36,**271–307.

Lasaga A. C. (1981) Transition state theory. *Rev. Min.* **8,** 135–169.

Lasaga A. C. (1984) Chemical kinetics of water-rock interactions. *J. Geophys. Res.* **89,** 4009–4025.

Leonards G. A. (1962) Engineering properties of soils. In *Foundation Engineering* (ed. G. A. Leonards), pp. 66–240. McGraw-Hill.

Lichtner P. C. (1988) The quasi stationary state approximation to coupled mass transport and fluid-rock interaction in porous media. *Geochim. Cosmochim. Acta* **52,** 143–165.

Lichtner P. C. (1996) Continuum formulation of multicomponent-multiphase reactive transport. *Rev. Min.* **34,** 1–81.

Lindquist W. B., Lee S. M., Coker D. A., Jones K. W., and Spanne P. (1996) Medial axis analysis of void structure in three-dimensional tomographic images of porous media. *J. Geophys. Res.* **101,** 8297–8310.

Lock P. A., Jing X., and Zimmerman R. W. (2002) Predicting permeability of sandstone from image analysis of pore structure. *J. Appl. Phys.* **92,** No.10., 6311–6319.

Luttge A., Bolton E. W., and Lasaga A. C. (1999) An interferometric study of the dissolution kinetics of anorthite: The role of reactive surface area. *Am. J. Sci.* **299,** 652–678.

Mok U., Bernabe Y. and Evans B. (2002) Permeability, porosity and pore geometry of chemically altered porous silica glass. *J. Geophys. Res.* **107**, ECV 4–1 –ECV 4–10.

Oelkers E. H. (1996) Summary and review of the physical and chemical properties of rocks and fluids. *Rev. Min.* **34,** 131–191.

Oelkers E. H. (2001) A general kinetic description of multi-oxide silicate mineral and glass dissolution. *Geochim. Cosmochim. Acta* **65,** 3703–3719.

Oelkers E. H. (2002) The surface area of rocks and minerals. In *Proceedings of the Arezzo Seminar on Fluid Geochemistry* (eds. L. Martini and G. Ottonello), pp. 18–30. Pacini Edtiore.

Oelkers E. H., Bjørkum P. A., and Murphy W. M. (1996) A petrographic and computational investigation of quartz cemention and porosity reduction in North Sea sandstones. *Am. J. Sci.* **296,** 420–452.

Ortoleva P., Merino E., Moore C., and Chadam J. (1987) Geochemical self-organization I: Reaction-transport feedbacks and modeling approach. *Am. J. Sci.* **287,** 979–1007.

Panda M. N. and Lake L. W. (1994) Estimation of single phase permeability from parameters of particle size distribution. *AAPG Bull.* **78,** 1028–1039.

Schwartz L. M., Martys N., Bentz N., Garboczi E. J., and Torquato S. (1993) Cross-property relations and permeability estimation in model porous media. *Phys. Rev. E* **48,** 4584–4591.

Sevougian S. D., Lake L. W. and Schechter R. S. (1992) A new geochemical simulator to design more effective sandstone acidizing treatments. Presented at the 67th Annual Technical Conference and Exhibition of the Society of Petroleum Engineers of AIME. Paper SPE24780. SPE.

Shmonov V. M., Vitovtova V. M., and Zarubina I. V. (1995) Permeability at elevated temperatures and pressures. In *Fluids in the Crust—Equilibrium and Transport Properties* (eds. K. I. Shmulovich, B. W.D. Yardley, and G. G. Gonchar), pp. 285–314. Chapman-Hill.

Sisavath S., Jing X., and Zimmerman R. W. (2001) Laminar flow through irregularly-shaped pores in sedimentary rocks. *Transport Porous Media* **45,** 41–62.

Steefel C. I. and Lasaga A. C. (1994) A coupled model for transport of multiple chemical species and kinetic precipitation/dissolution reactions with application to reactive flow in single phase hydrothermal systems. *Am. J. Sci.* **294,** 529–592.

Steefel C. I. MacQuarrie (1996) Approaches to modeling of reactive transport in porous media. *Rev. Min.* **34,** 83–129.

Wolery T. J. (1983) *EQ3NR, a Computer Program for Geochemical Aqueous Speciation-Solubility Calculations: User's Guide and Documentation* UCRL-53414. Lawrence Livermore National Laboratory.

Wolery T. J. (1992) *EQ3NR, a Computer Program for Geochemical Aqueous Speciation-Solubility Calculations: Theoretical Manual, User's Guide and Related Documentation* Version 7.0. UCRL-MA-110662 Pt. 3. Lawrence Livermore National Laboratory.

Wolery T. J. and Daveler S. A. (1992) *Eqn. 6, a Computer Program for Reaction Path Modeling of Aqueous Geochemical Systems: Theoretical Manual, User's Guide and Related Documentation* Version 7.0. UCRL-MA-110662 Pt. 4. Lawrence Livermore National Laboratory.

Zaytsev I. D. and Aseyev G. G. (1992) *Properties of Aqueous Solutions of Electrolytes*. CRC Press.